



VYSOKÉ UČENÍ TECHNICKÉ V BRNĚ

BRNO UNIVERSITY OF TECHNOLOGY

FAKULTA STROJNÍHO INŽENÝRSTVÍ

FACULTY OF MECHANICAL ENGINEERING

ÚSTAV MECHANIKY TĚLES, MECHATRONIKY A BIOMECHANIKY

INSTITUTE OF SOLID MECHANICS, MECHATRONICS AND BIOMECHANICS

VÝPOČTOVÉ MODELOVÁNÍ VLIVU PORUCH ŠÍŘENÍ VZRUCHU NA KONTRAKCI LEVÉ SRDEČNÍ KOMORY

COMPUTATIONAL STUDY OF THE IMPACT OF DISORDERS IN EXCITATION PROPAGATION ON LEFT VENTRICULAR CONTRACTION

TEZE DIZERTAČNÍ PRÁCE

DOCTORAL THESIS SUMMARY

AUTOR PRÁCE

AUTHOR

Ing. Jiří Vaverka

ŠKOLITEL

SUPERVISOR

prof. Ing. Jiří Burša, Ph.D.

BRNO 2022

Keywords

heart, left ventricle, finite element method, conduction system, left bundle branch, monodomain equation, hyperelasticity

Klíčová slova

srdce, levá komora, metoda konečných prvků, převodní systém, levé Tawarovo raménko, monodoménová rovnice, hyperelastická

The full version of the thesis is archived at:
Institute of Solid Mechanics, Mechatronics and Biomechanics
Faculty of Mechanical Engineering
Brno University of Technology
Technická 2896/2
616 69 Brno

Contents

- 1 Scope of thesis** **5**
- 2 Motivation and objectives** **5**
- 3 Calculation of electrical activation maps** **7**
 - 3.1 Computational domain, finite-element mesh 7
 - 3.2 Discretization and linearization of the monodomain equation 8
 - 3.3 Specification of simulated conditions 11
 - 3.4 Results 13
- 4 Simulations of ventricular contraction** **14**
 - 4.1 Passive mechanical properties of myocardium 14
 - 4.2 Inclusion of prestress 17
 - 4.3 Modeling of fibre contraction 19
 - 4.4 Specification of simulated conditions 19
 - 4.5 Results 20
- 5 Conclusion** **27**
- References** **28**
- Curriculum vitae** **32**
- Abstract** **33**

1 Scope of thesis

This thesis deals with computational modeling of electrophysiology and mechanics of the left ventricle (LV) of the heart. These two fields of study are closely related in the context of cardiac physiology because contraction is induced by electrical activation. It follows that electrical disturbances in LV affect also its mechanical function, more precisely its ability to generate blood pressure inside the ventricle and, consequently, to eject sufficient amount of blood into aorta. This work is focused on one of the most common pathological conditions affecting the electrical activation of LV – the left bundle branch block (LBBB). Modern computational methods and various mathematical models, describing different aspects of LV function, are integrated together in order to investigate the impact of LBBB on LV function.

2 Motivation and objectives

The heart is equipped with a network of specialized cells that are responsible for coordinated propagation of electrical signal through the heart. They constitute the *conduction system* of the heart. One of the components of the conduction system is the *left bundle branch* which is responsible for the electrical activation of the LV. The left bundle branch splits into a fine network of Purkinje fibres which rapidly distribute electrical impulse through the internal (endocardial) surface of the ventricle. Because of high conduction velocity in the left bundle branch and the Purkinje network, the resulting contraction of a healthy ventricle is fairly synchronous.

The normal electrical activation process is disrupted when the left bundle branch ceases to conduct the electrical impulse which can arise as a consequence of various anatomical or functional lesions in the ventricle (e.g. infarction or cardiomyopathy) [1]. Such conduction defect is called the *left bundle branch block*. When the block occurs, the LV is activated by electrical impulse originating in the right ventricle. The activation wave then propagates from the right side of the interventricular septum to the left through the LV muscular tissue (myocardium) which conducts with much lower velocities than the specialized conduction system. Consequently, the electrical activation of LV is prolonged because of the LBBB.

The disrupted activation pattern necessarily leads to asynchronous and less efficient contraction of LV [2]. In order to evaluate the impact of LBBB on LV function, several clinical studies have compared LV ejection fraction¹ in patients with LBBB against healthy individuals; e.g. [4, 5, 6, 7, 8]. Their results are summarized in Table 1 and illustrated in Fig. 1. It can be seen that the results are not entirely conclusive because the reported decrease in mean ejection fraction ranges from 4 % in [5, 8] to as much as 14.2 % in [6]. Since the LBBB is usually accompanied by other cardiovascular diseases [1], it is possible that the large decrease observed by some authors could be partially caused by some other diseases and, consequently, that the impact of the LBBB was overestimated in their studies.

Besides reducing the pumping ability of the ventricle, the LBBB was also seen to alter the motions of the ventricle [9, 10] and it is hypothesized that the asynchronous

¹Ejection fraction is the volume fraction of blood ejected from the LV per one beat, expressed in percents. It is the most widely used measure of the pumping efficiency of the ventricle and an indicator of the severity of heart failure [3].

contraction due to the LBBB overloads some regions of the ventricular muscle which can cause tissue remodeling [2].

With regard to the above facts, **this thesis aims (i) to develop an electromechanical finite-element (FE) model of human left ventricle capable of simulating ventricular contraction under different conditions and (ii) to employ the model to investigate the impact of isolated LBBB on ventricular hemodynamics, kinematics and wall stress.**

Table 1: Ejection fractions in healthy individuals (Control) and patients with isolated left bundle branch block (LBBB) from 5 clinical studies. Values are means \pm SD, n is the number of subjects.

	Control	LBBB
Grines et al. (1989) [4]	62 ± 5 % ($n = 10$)	54 ± 7 % ($n = 18$)
Özdemir et al. (2001) [5]	68 ± 6 % ($n = 65$)	64 ± 6 % ($n = 45$)
Valenti et al. (2012) [6]	63.1 ± 5.3 % ($n = 10$)	48.9 ± 6.6 % ($n = 39$)
Akhtari et al. (2018) [7]	68 ± 6 % ($n = 18$)	56 ± 7 % ($n = 18$)
Aalen et al. (2019) [8]	60 ± 4 % ($n = 11$)	56 ± 6 % ($n = 11$)

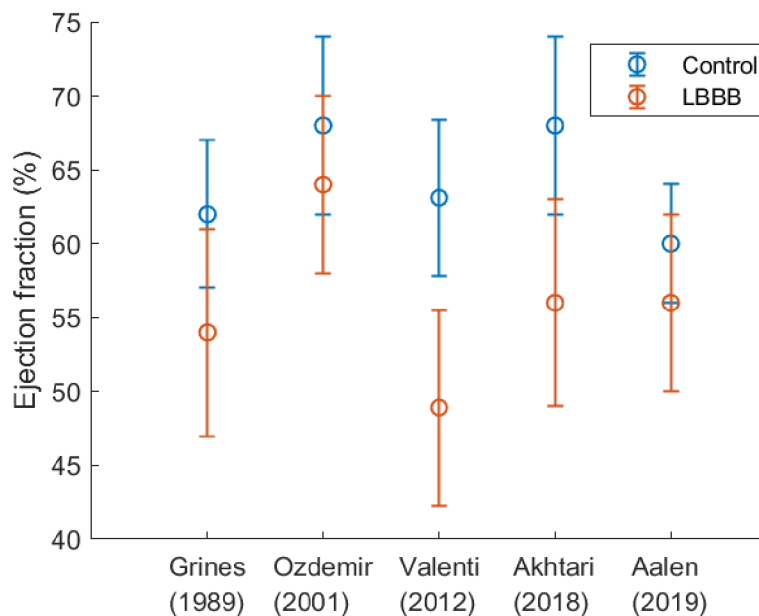


Fig. 1: Mean ejection fractions \pm SD in healthy individuals (Control) and patients with isolated left bundle branch block (LBBB) reported by Grines et al. [4], Özdemir et al. [5], Valenti et al. [6], Akhtari et al. [7] and Aalen et al. [8].

This thesis extends the previous research [11, 12] on some closely related topics which was conducted by me, my supervisor Jiří Burša and our colleagues from Masaryk University. Within this research, we investigated the importance of experimentally observed transmural differences in electromechanical delay and myocyte shortening velocity for LV function [11] and then we studied the impact of decreased conduction velocity on LV pressure rise during isovolumic contraction [12]. The main results of the latter study were that 50% decrease in transmural conduction velocity prolongs the isovolumic contraction by 18 % and decreases slightly the maximum rate of left ventricular pressure rise. Although these results practically fulfilled the originally formulated goals of my dissertation, we

eventually decided to develop a new, much more elaborated model capable of simulating the whole cardiac cycle. Also, we turned our attention to investigating the LBBB which is nowadays more extensively discussed in literature than the reduced conductivity of myocardium.

3 Calculation of electrical activation maps

In the simulations of ventricular contraction, it is always necessary to directly prescribe the spatial distribution of the beginning of contraction in the computational domain Ω . Since the onset of contraction is determined by the time of electrical activation, each simulation of mechanics must be preceded by a simulation of electrical activity from which the distribution of electrical activation times (activation map) can be obtained.

3.1 Computational domain, finite-element mesh

An essential requirement for mathematical solution of any physical problem described in space is a specification of the spatial computational domain Ω . In this work, it was defined on the basis of the publicly available¹ model of LV geometry which was created by Bai et al. [13]. A slightly modified version of the model is shown in Fig. 2A and its spatial discretization by quadratic tetrahedral isoparametric elements is shown in Fig. 2B. The mesh in the figure will be denoted as \mathcal{T}_h where $h = 2$ mm is the maximum diameter of the elements in \mathcal{T}_h . A generic element of \mathcal{T}_h will be denoted as K .

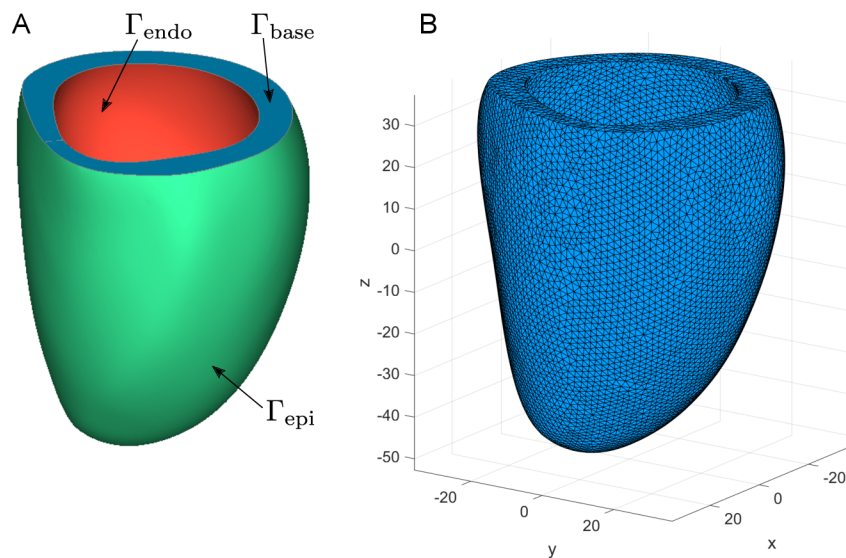


Fig. 2: (A) The computational domain Ω which represents normal human LV at the end of diastole. Its boundary, $\partial\Omega$, is formed by endocardial (Γ_{endo}), epicardial (Γ_{epi}) and basal (Γ_{base}) surfaces. (B) A quadratic tetrahedral mesh with maximum element diameter $h = 2$ mm. This mesh was used in the simulations of electrophysiology, as well as in the subsequent simulations of mechanics.

¹<http://wp.doc.ic.ac.uk/wbai/data>

3.2 Discretization and linearization of the monodomain equation

Propagation of electrical activation in myocardial tissue is mathematically described by the *monodomain equation* [14] which in this work was used in the following form:

$$\frac{\partial v}{\partial t} = \operatorname{div}(\mathbf{D}\nabla v) - J_{\text{ion}} \circ v + J_{\text{stim}}. \quad (3.1)$$

The above equation is defined in terms of the normalized dimensionless potential v (ranging from 0 to 1), time t , the diffusion tensor \mathbf{D} , the stimulus current J_{stim} and the artificial ionic current J_{ion} which is defined by:

$$J_{\text{ion}}(v) := \begin{cases} \alpha(v^2 - v) & \text{for } v \in (0, 1) \\ 0 & \text{for } v \in \mathbb{R} \setminus (0, 1), \end{cases} \quad (3.2)$$

where $\alpha > 0$ is a parameter controlling the rate of growth of v . The definition (3.2) is not intended to represent any real ionic current flowing through the cellular membrane; it was formulated in order to reduce the computational demands of the monodomain equation which are extremely high if a real ionic model is used. The stimulus current, J_{stim} , serves to initiate the growth of v in selected portions of the model (first activated regions). It is usually prescribed only during the first few milliseconds of simulation; after that the activation propagates without the need of any external source. Potential v in (3.1) is considered to be a mapping of the form $v: \langle 0, T \rangle \times \Omega \rightarrow \mathbb{R}$ where Ω is the spatial domain and $\langle 0, T \rangle$ is the time interval. The diffusion tensor \mathbf{D} governs the velocity of propagation of activation in three orthogonal directions (propagation is assumed orthotropic [15]). It can be written as [16]

$$\mathbf{D} := D_{\mathbf{f}} \mathbf{f} \otimes \mathbf{f} + D_{\mathbf{s}} \mathbf{s} \otimes \mathbf{s} + D_{\mathbf{n}} \mathbf{n} \otimes \mathbf{n}, \quad (3.3)$$

where $D_{\mathbf{f}}$, $D_{\mathbf{s}}$, $D_{\mathbf{n}}$ are diffusion coefficients (or diffusivities) in the three material directions depicted in Fig. 3.

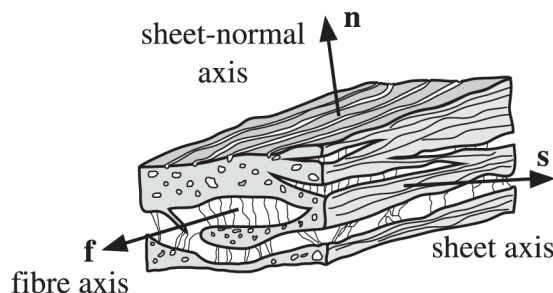


Fig. 3: A scheme of the 3-dimensional structure of ventricular myocardium. Parallel muscle fibres are represented by vector \mathbf{f} . They are arranged in layers, called *sheets*. Sheet vector \mathbf{s} lies in the plane of the sheet and is perpendicular to \mathbf{f} . Sheet-normal vector \mathbf{n} is perpendicular to the other two vectors. (Adopted from [17] and modified).

If we assume that the pseudo-potential v is initially zero (initial condition) and, following [18, 14], that no current flows across the boundary during the whole time interval (Neumann boundary condition), we can formulate the following initial-boundary value

problem [19]: Find $v: \langle 0, T \rangle \times \Omega \rightarrow \mathbb{R}$ such that

$$\begin{cases} \frac{\partial v}{\partial t} = \operatorname{div}(\mathbf{D}\nabla v) - J_{\text{ion}} \circ v + J_{\text{stim}} & \text{in } (0, T) \times \Omega \\ (\mathbf{D}\nabla v) \cdot \mathbf{n} = 0 & \text{in } (0, T) \times \partial\Omega \\ v(0) = 0 & \text{in } \Omega, \end{cases} \quad (3.4)$$

where \mathbf{n} is the outward unit normal to the boundary $\partial\Omega$.

The finite-element solution of (3.4) requires to develop the *weak formulation* of the problem. To that end, we must express the governing equation (3.4)₁ at a particular time t , multiply the result by a *test function* u and integrate over Ω [20]. After some manipulation of the resulting expression (using the product rule for divergence, the divergence theorem and the boundary condition (3.4)₂), the weak formulation of the original problem (3.4) can be expressed as follows [19]: Find $v: \langle 0, T \rangle \rightarrow H^1(\Omega)$ such that $v(0) = 0$ and for each $t \in (0, T)$ it holds that

$$\int_{\Omega} \dot{v}(t) u + \int_{\Omega} \nabla u \cdot (\mathbf{D}\nabla v(t)) = - \int_{\Omega} (J_{\text{ion}} \circ v(t)) u + \int_{\Omega} J_{\text{stim}}(t) u \quad \forall u \in H^1(\Omega), \quad (3.5)$$

where $H^1(\Omega)$ is the first-order Sobolev space.

The weak formulation (3.5) can be approximated by replacing $H^1(\Omega)$ with its finite-dimensional subspace \mathcal{V}_h . For the particular case of the isoparametric mesh \mathcal{T}_h in Fig. 2B, \mathcal{V}_h is the space spanned by the standard Lagrangian basis functions $\psi_1, \dots, \psi_{N_h}$, where N_h is the number of nodes in \mathcal{T}_h (see [21] for more details). The basis functions are characterized by the property:

$$\psi_i(\mathbf{a}_j) = \delta_{ij} \quad \forall i, j \in \{1, 2, \dots, N_h\}, \quad (3.6)$$

where \mathbf{a}_j is the j -th node of \mathcal{T}_h . Once $H^1(\Omega)$ is replaced by \mathcal{V}_h , the following expansions can be written:

$$v(t) = \sum_{j=1}^{N_h} v_j(t) \psi_j, \quad (3.7)$$

$$\dot{v}(t) = \sum_{j=1}^{N_h} \dot{v}_j(t) \psi_j, \quad (3.8)$$

$$\nabla v(t) = \sum_{j=1}^{N_h} v_j(t) \nabla \psi_j, \quad (3.9)$$

$$J_{\text{stim}}(t) = \sum_{j=1}^{N_h} J_{\text{stim},j}(t) \psi_j, \quad (3.10)$$

$$J_{\text{ion}} \circ v(t) = \sum_{j=1}^{N_h} J_{\text{ion}}(v_j(t)) \psi_j. \quad (3.11)$$

Expressions (3.7)–(3.11) can now be inserted into eq. (3.5) which leads to the following semi-discrete finite element problem [19]: Find a family of functions v_1, \dots, v_{N_h} from

$\langle 0, T \rangle$ to \mathbb{R} satisfying $v_j(0) = 0$, such that the mapping $v : \langle 0, T \rangle \rightarrow \mathcal{V}_h$ defined by $v(t) := \sum_{j=1}^{N_h} v_j(t) \psi_j$ satisfies, for all $t \in (0, T)$, the following condition:

$$\sum_{j=1}^{N_h} M_{ij} \dot{v}_j(t) + \sum_{j=1}^{N_h} K_{ij} v_j(t) = - \sum_{j=1}^{N_h} M_{ij} J_{\text{ion}}(v_j(t)) + \sum_{j=1}^{N_h} M_{ij} J_{\text{stim},j}(t) \quad \forall i \in \{1, \dots, N_h\}, \quad (3.12)$$

where

$$M_{ij} := \int_{\Omega} \psi_i \psi_j \quad \forall i, j \in \{1, \dots, N_h\}, \quad (3.13)$$

$$K_{ij} := \int_{\Omega} \nabla \psi_i \cdot (\mathbf{D} \nabla \psi_j) \quad \forall i, j \in \{1, \dots, N_h\}. \quad (3.14)$$

The problem (3.12) is a system of N_h nonlinear ordinary differential equations for determination of the unknown functions v_1, \dots, v_{N_h} . It can be alternatively expressed in matrix form:

$$\mathbf{M} \dot{\mathbf{v}}(t) + \mathbf{K} \mathbf{v}(t) = -\mathbf{M} \mathbf{J}_{\text{ion}}(\mathbf{v}(t)) + \mathbf{M} \mathbf{J}_{\text{stim}}(t), \quad (3.15)$$

where

$$\mathbf{M} := [M_{ij}]_{i,j=1}^{N_h}, \quad (3.16)$$

$$\mathbf{K} := [K_{ij}]_{i,j=1}^{N_h}, \quad (3.17)$$

$$\mathbf{v}(t) := [v_1(t), \dots, v_{N_h}(t)]^{\top}, \quad (3.18)$$

$$\dot{\mathbf{v}}(t) := [\dot{v}_1(t), \dots, \dot{v}_{N_h}(t)]^{\top}, \quad (3.19)$$

$$\mathbf{J}_{\text{ion}}(\mathbf{v}(t)) := [J_{\text{ion}}(v_1(t)), \dots, J_{\text{ion}}(v_{N_h}(t))]^{\top}, \quad (3.20)$$

$$\mathbf{J}_{\text{stim}}(t) := [J_{\text{stim},1}(t), \dots, J_{\text{stim},N_h}(t)]^{\top}. \quad (3.21)$$

Equation (3.15) can be discretized in time using the backward Euler method [20]. One step of solution from time t_k to t_{k+1} is then described by:

$$\mathbf{M} \frac{\mathbf{v}_{k+1} - \mathbf{v}_k}{\Delta t} + \mathbf{K} \mathbf{v}_{k+1} = -\mathbf{M} \mathbf{J}_{\text{ion}}(\mathbf{v}_{k+1}) + \mathbf{M} \mathbf{J}_{\text{stim}}, \quad (3.22)$$

where \mathbf{v}_{k+1} is the vector of unknown nodal potentials, \mathbf{J}_{stim} is a vector of nodal stimuli at t_{k+1} and \mathbf{J}_{ion} is a mapping from \mathbb{R}^{N_h} to itself defined by:

$$\mathbf{J}_{\text{ion}}(\mathbf{v}) := [J_{\text{ion}}(v_1), \dots, J_{\text{ion}}(v_{N_h})]^{\top} \quad \forall \mathbf{v} = [v_1, \dots, v_{N_h}]^{\top} \in \mathbb{R}^{N_h}. \quad (3.23)$$

From the computational viewpoint, it is important that \mathbf{J}_{ion} is nonlinear, owing to the nonlinear definition of J_{ion} by (3.2). Consequently, the discretized equation (3.22) must be solved iteratively using the Newton-Raphson procedure. The linearized form of (3.22), which must be solved in each iteration, can be expressed as

$$\left(\mathbf{M} (\nabla_{\mathbf{v}} \mathbf{J}_{\text{ion}}) + \frac{1}{\Delta t} \mathbf{M} + \mathbf{K} \right) \mathbf{a} = -\mathbf{M} \left(\mathbf{J}_{\text{ion}}(\mathbf{v}) - \mathbf{J}_{\text{stim}} + \frac{\mathbf{v} - \mathbf{u}}{\Delta t} \right) - \mathbf{K} \mathbf{v}, \quad (3.24)$$

where $\mathbf{u} = \mathbf{v}_k$ is the converged solution at time t_k , \mathbf{v} is the last (non-converged) estimate of the solution at t_{k+1} , \mathbf{a} is an unknown increment that should improve the last estimate \mathbf{v} (i.e. bring it closer to the exact solution), and $\nabla_{\mathbf{v}} \mathbf{J}_{\text{ion}}$ is an $N_h \times N_h$ diagonal matrix with derivatives of J_{ion} on its main diagonal.

The iterative solution based on eq. (3.24) was implemented in Matlab. Details about the implementation (evaluation of integrals, assemblage of matrices, etc.) can be found in the full version of the thesis.

3.3 Specification of simulated conditions

Since the spread of activation is orthotropic [15], it was necessary to rotate the element coordinate systems of all elements in mesh so that the coordinate axes are aligned with the local microstructural directions \mathbf{f} , \mathbf{s} , \mathbf{n} . Experiments showed [22] that \mathbf{f} and \mathbf{s} directions are approximately tangent to the wall and that the angle between \mathbf{f} and the local circumferential direction changes approximately linearly between endocardium and epicardium from $+60^\circ$ (right-hand helix) to -60° (left-hand helix). On the basis of these findings, an algorithm was written in Matlab which assigned to each element in the mesh its own element coordinate system with properly aligned axes. The algorithm is described in detail in Sec. 4.11 of the full version of the thesis.

The specialized ventricular conduction system was represented by thin fast-conducting layers \mathcal{T}_h^L and \mathcal{T}_h^R which are shown in Fig. 4. The position and extent of these layers were defined on the basis of the three-dimensional reconstructions of the conduction system published by Stephenson et al. [23]. Within the layers, four sets of nodes were selected (S_h^{ant} , S_h^{sep} , S_h^{pos} and S_h^{R} in Fig. 4) in such a manner that their locations correspond with the early-activated areas in LV described by Durrer et al. [24]. The spread of activation in the simulations was initiated by electrical stimulus applied to the nodes in these sets.

In order to determine suitable values of diffusion coefficients, several trial simulations were performed on meshes with simple geometry and small number of elements. All trial simulations used the same element size $h = 2$ mm, time step $\Delta t = 0.5$ ms and rate parameter $\alpha = 0.1$ ms $^{-1}$ (eq. (3.2)). The same values were used in the subsequent simulations of LV activation. A particular node was considered activated when its dimensionless potential v reached 0.5. Final chosen values of the diffusion coefficients, producing approximately the velocities measured in experiments [15, 25], are given in Table 2.

Table 2: Selected (tuned) diffusivities (1st column) and the corresponding approximate conduction velocities (2nd column) for fibre (f), sheet (s) and sheet-normal (n) directions in myocardium and for the fast-conducting layers (fc).

$D_f := 2.5 \text{ mm}^2 \cdot \text{ms}^{-1}$	$v_f \approx 0.67 \text{ mm} \cdot \text{ms}^{-1}$
$D_s := 0.53 \text{ mm}^2 \cdot \text{ms}^{-1}$	$v_s \approx 0.30 \text{ mm} \cdot \text{ms}^{-1}$
$D_n := 0.18 \text{ mm}^2 \cdot \text{ms}^{-1}$	$v_n \approx 0.17 \text{ mm} \cdot \text{ms}^{-1}$
$D_{fc} := 28 \text{ mm}^2 \cdot \text{ms}^{-1}$	$v_{fc} \approx 2.3 \text{ mm} \cdot \text{ms}^{-1}$

Two simulations of the electrical activation of LV were performed, the first represented the ventricle with intact left bundle branch (control simulation), while the second represented the ventricle with disabled branch (LBBB simulation).

In the control simulation, both \mathcal{T}_h^L and \mathcal{T}_h^R served as fast-conducting layers. The elements contained in these layers had prescribed diffusion coefficients D_{fc} , D_{fc} and D_n respectively in \mathbf{f} , \mathbf{s} and \mathbf{n} directions (\mathbf{n} points in a direction transverse to the fast-conducting layers in which rapid propagation cannot be expected). In all other elements, D_f , D_s and D_n were prescribed in \mathbf{f} , \mathbf{s} and \mathbf{n} directions, respectively. The stimulus currents were applied according to Table 3. Values of stimuli as well as durations of their application were determined more or less by trial and error. The goal was to achieve synchronous activation of S_h^{ant} , S_h^{sep} and S_h^{pos} in the control simulation and to delay the activation of S_h^{R} by about 10 ms [24] relative to the former three sets.

In the LBBB simulation, the rapid conduction with coefficients D_{fc} , D_{fc} and D_n was prescribed only in \mathcal{T}_h^R ; all other elements (including those in \mathcal{T}_h^L) conducted with

coefficients D_f , D_s and D_n . Stimulus was applied only to S_h^R .

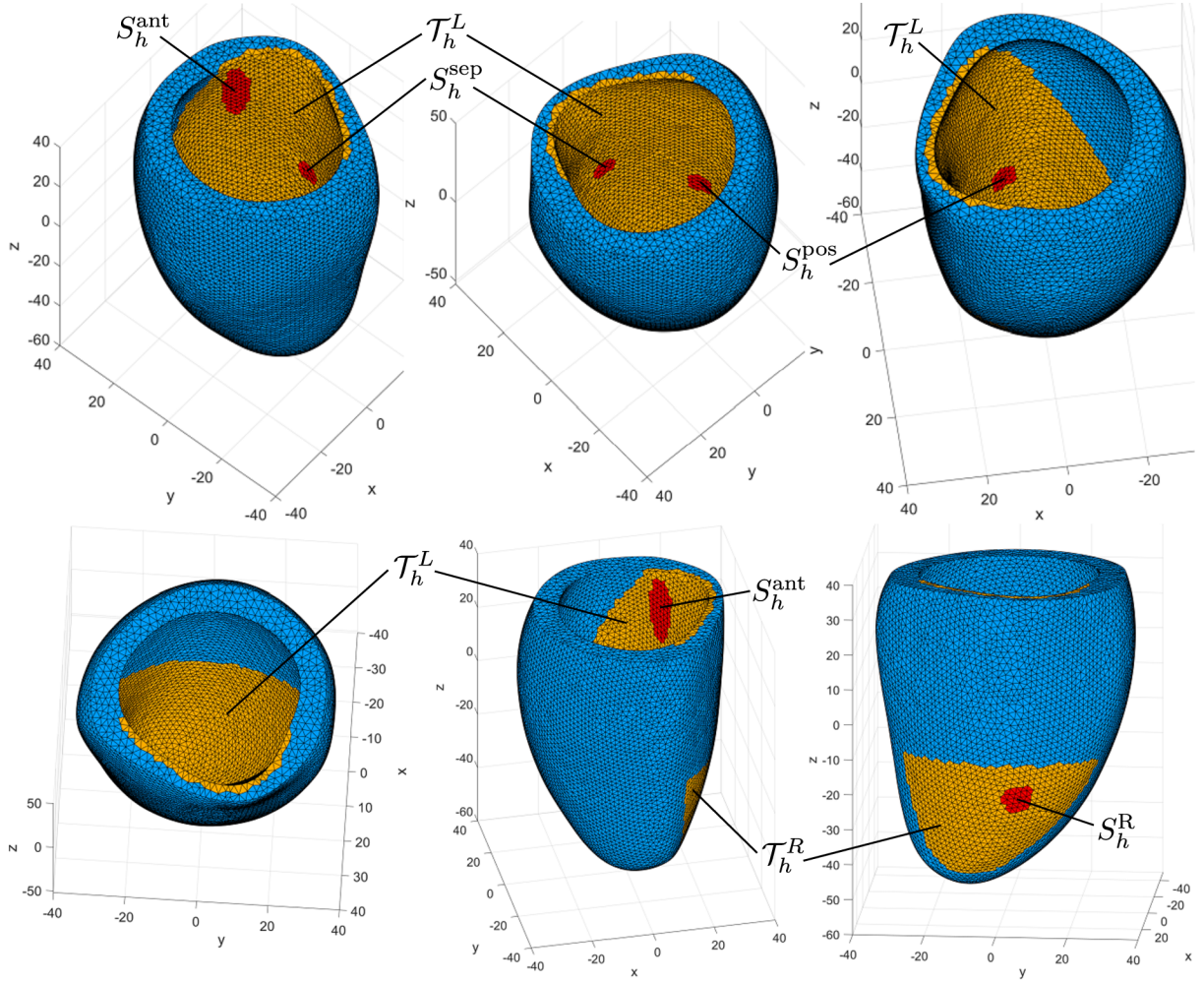


Fig. 4: Fast-conducting layers (orange) and early-activated areas (red) in the model of left ventricle. Fast-conducting layers represent Purkinje fibres originating from the left bundle branch (layer \mathcal{T}_h^L) and the right bundle branch (layer \mathcal{T}_h^R). Layer \mathcal{T}_h^L covers lower parts of the left ventricular endocardium and the whole left septal surface. Layer \mathcal{T}_h^R covers low right septal surface. Early-activated areas are contained in the layers. Surface nodes inside the areas form sets S_h^{ant} , S_h^{sep} , S_h^{pos} and S_h^R on which electrical stimulus can be applied in simulations.

Table 3: Values of stimuli, J_{stim} , and time periods of their application, t_{stim} , in the control simulation and in the simulation of LBBB. Stimuli were prescribed separately to nodes in sets S_h^{ant} , S_h^{sep} , S_h^{pos} and S_h^R (see Fig. 4).

	S_h^{ant}		S_h^{sep}		S_h^{pos}		S_h^R	
	J_{stim} (ms^{-1})	t_{stim} (ms)	J_{stim} (ms^{-1})	t_{stim} (ms)	J_{stim} (ms^{-1})	t_{stim} (ms)	J_{stim} (ms^{-1})	t_{stim} (ms)
Control	1.0	$\langle 0, 50 \rangle$	2.0	$\langle 0, 50 \rangle$	1.85	$\langle 0, 50 \rangle$	1.6	$\langle 10, 60 \rangle$
LBBB	0	–	0	–	0	–	1.6	$\langle 0, 50 \rangle$

3.4 Results

Both simulations specified in the previous section were realized in software Matlab R2021b in which the iterative algorithm based on the finite element method was implemented. All systems of linear equations were solved using Matlab built-in direct solver.

The total calculated activation time in the control simulation was 102.5 ms which is within the range of normal values [1]. Total activation time in the LBBB simulation was 153.5 ms which means that complete depolarization required 51 ms more than in the control case (50% increase). This prolongation corresponds with values reported in literature [8, 26]. Activation maps reconstructed from the calculated nodal activation times are displayed in Fig. 5.

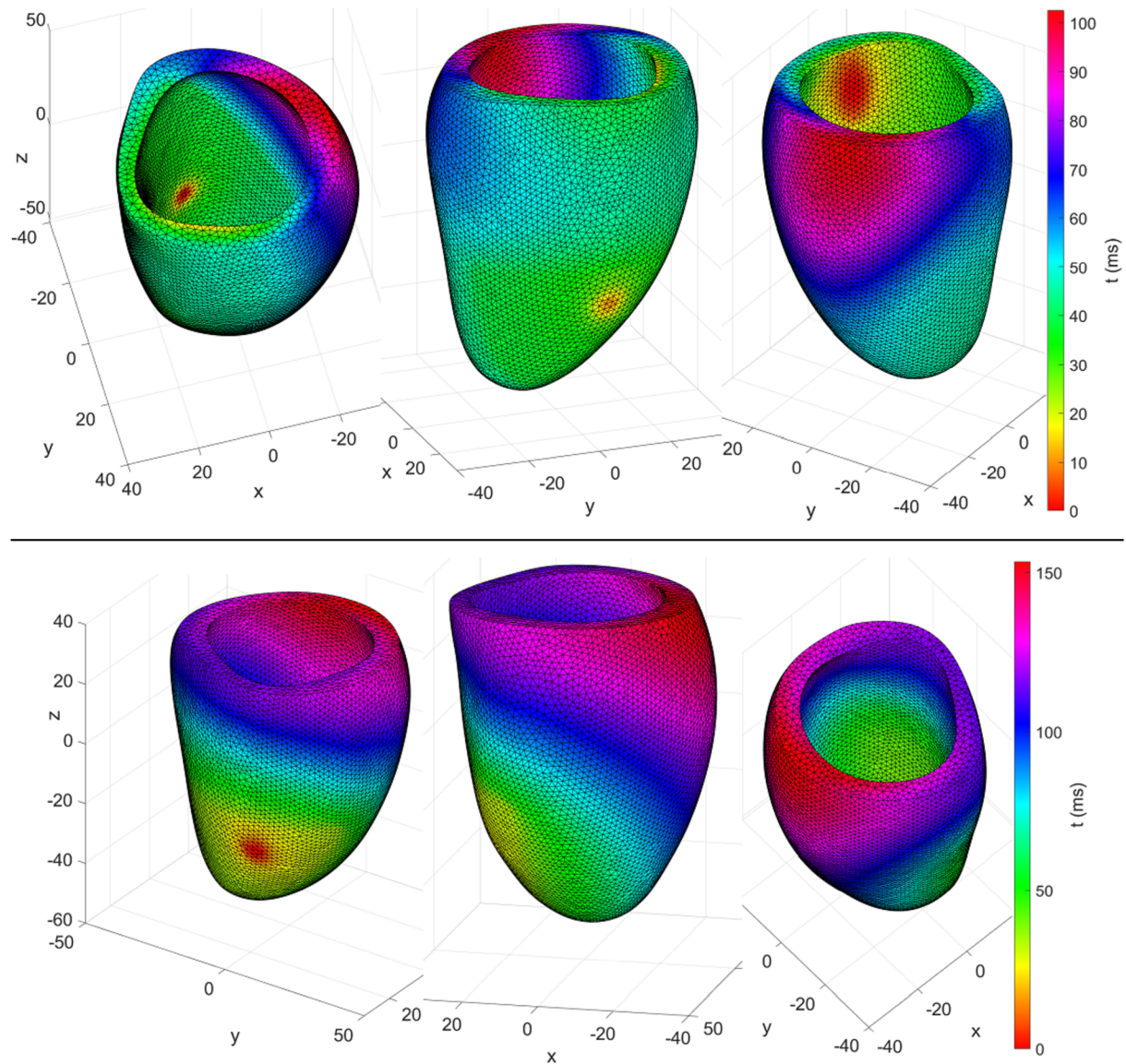


Fig. 5: Activation times measured from the onset of activation in the model; i.e. $t = 0$ ms marks the instant of the first occurrence of $v > 0.5$. Top row: control simulation, bottom row: LBBB simulation.

Calculated nodal activation times from both simulations were interpolated into elements' centroids and the resulting values were saved in order to be used to distribute the onset of contraction in the subsequent simulations of ventricular mechanics.

4 Simulations of ventricular contraction

The same FE mesh which was used to simulate the electrical activation (Fig. 2B) was used also in the simulations of ventricular contraction. However, contrary to the simulations of electrophysiology, which were completely programmed in Matlab, simulations of mechanics were realized in commercial FE software Ansys Mechanical APDL 2021 R2.

4.1 Passive mechanical properties of myocardium

Passive mechanical properties of myocardium (stress-strain relations) are most often determined by quasi-static biaxial extension tests [27, 28] or by simple shear tests [29, 28]. Biaxial tests are typically performed with thin squared specimens excised parallel to the ventricular wall, as shown in Fig. 6A. Two parallel edges of the specimens are always aligned with the mean-fibre direction \mathbf{f} , while the other two correspond to a cross-fibre direction \mathbf{s} . However, biaxial tests alone are not sufficient for a complete characterization of the passive properties of myocardium. In order to capture the response in three independent directions, biaxial tests must be complemented by triaxial simple shear tests [28]. These are performed on small cubic specimens with edges aligned with the local \mathbf{f} , \mathbf{s} , \mathbf{n} directions. Fig. 6B shows six possible shear modes in which the cubic specimens can be deformed.

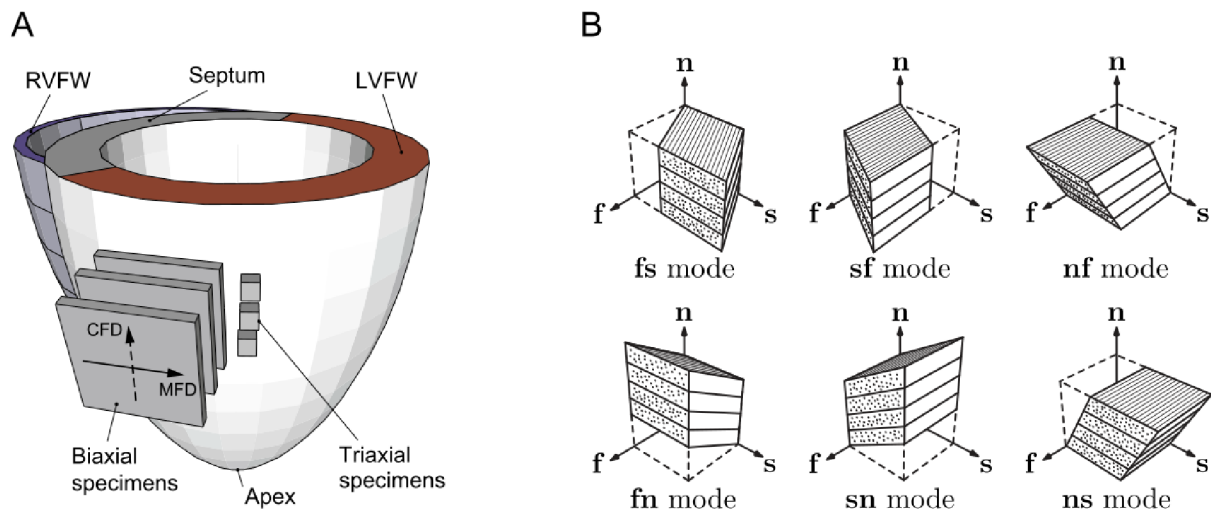


Fig. 6: (A) Schematic representation of ventricles showing locations from which Sommer et al. [28] excised squared biaxial specimens and cubic triaxial shear specimens. MFD: mean-fibre direction, CFD: cross-fibre direction, LVFW: left ventricular free wall, RVFR: right ventricular free wall. (B) Six possible simple shear modes for cubic myocardial specimens (e.g., the \mathbf{fs} mode means simple shear in which the face with normal vector \mathbf{f} is shifted in the direction \mathbf{s}). Figure adopted from [28] and modified.

Currently, the only study which provide results from both biaxial and simple shear tests of human ventricular myocardium is that by Sommer et al. (2015) [28]. The shear protocol of the study included all six possible simple shear modes and the biaxial testing protocol included five different strain ratios between the mean-fibre direction and the cross-fibre direction, namely: 0.5 : 1, 0.75 : 1, 1 : 1 (equibiaxial loading), 1 : 0.75, 1 : 0.5. These experimental data were used in this thesis to estimate the material parameters a ,

b , $a_{\mathbf{f}}$, $b_{\mathbf{f}}$, $a_{\mathbf{fs}}$, $b_{\mathbf{fs}}$ of the strain-energy function

$$\begin{aligned}\Psi_{\text{alt}} &:= \Psi_{\text{iso}} + \Psi_{\mathbf{f}} + \Psi_{\mathbf{fs}} + \Psi_{\text{vol}} \\ &= \frac{a}{2b}(\exp(b(\bar{I}_1 - 3)) - 1) + \frac{a_{\mathbf{f}}}{2b_{\mathbf{f}}}(\exp(b_{\mathbf{f}}(I_4 - 1)^2) - 1) + \frac{a_{\mathbf{fs}}}{2b_{\mathbf{fs}}}(\exp(b_{\mathbf{fs}}(K_1 - 1)^2) - 1) \\ &\quad + \frac{\kappa}{2}(J - 1)^2.\end{aligned}\tag{4.1}$$

Bulk modulus κ in the last term of the above definition was set equal to 1 MPa in order to achieve approximately incompressible behavior. Invariants J , \bar{I}_1 , I_4 , and K_1 in (4.1) are defined in terms of the deformation gradient \mathbf{F} , the right Cauchy-Green tensor $\mathbf{C} := \mathbf{F}^T \mathbf{F}$, its cofactor $\text{cof}(\mathbf{C}) := \det(\mathbf{C})\mathbf{C}^{-1}$, and the structural tensors $\mathbf{f} \otimes \mathbf{f}$ and $\mathbf{n} \otimes \mathbf{n}$ as follows [17, 30]:

$$J := \det(\mathbf{F}), \tag{4.2}$$

$$\bar{I}_1 := J^{-\frac{2}{3}} \text{tr}(\mathbf{C}), \tag{4.3}$$

$$I_4 := \text{tr}(\mathbf{C}(\mathbf{f} \otimes \mathbf{f})), \tag{4.4}$$

$$K_1 := \text{tr}(\text{cof}(\mathbf{C})(\mathbf{n} \otimes \mathbf{n})). \tag{4.5}$$

It can be shown that $\sqrt{I_4}$ is the local stretch of a material fibre aligned with \mathbf{f} and $\sqrt{K_1}$ is the local *areal* stretch of the material surface transverse to \mathbf{n} [31]. Thus the term $\Psi_{\mathbf{f}}$ in (4.1) represents the contribution of muscle fibres, while the term $\Psi_{\mathbf{fs}}$ represents the planar sheets.

The strain-energy function (4.1) is based on the well-known Holzapfel-Ogden model [17] but it employs the term $\Psi_{\mathbf{fs}}$ instead of a term with coupling invariant $I_8 := \text{tr}(\mathbf{C}(\mathbf{f} \otimes \mathbf{s}))$ used in the original model. As can be seen from Fig. 7, this new alternative model is very well capable of reproducing combined biaxial and simple shear responses, although it has also some drawbacks which are discussed in the full version of this thesis. The responses of the model plotted in Fig. 7 were obtained by solving a nonlinear least squares problem by the Gauss-Newton algorithm. The solution was performed in Matlab and the material parameters obtained from the solution are given in Table. 4 (penalty parameter κ was prescribed in advance and kept fixed during the fitting process).

Table 4: Values of material parameters for the strain-energy function (4.1) which were used to fit the corresponding stress response to the experimental data extracted from Sommer et al. [28].

a	b	$a_{\mathbf{f}}$	$b_{\mathbf{f}}$	$a_{\mathbf{fs}}$	$b_{\mathbf{fs}}$	κ
(kPa)	(-)	(kPa)	(-)	(kPa)	(-)	(kPa)
1.1672	6.4795	1.0270	38.8499	0.2807	11.6417	10^3

Hyperelastic model (4.1) was implemented into Ansys by means of the general material subroutine `UserMat` [32]. The two most important quantities that are needed for the implementation are the Cauchy stress tensor, $\boldsymbol{\sigma}$, and the Jaumann tangent stiffness tensor, \mathbf{c}^J , which are both derived in the full version of the thesis.

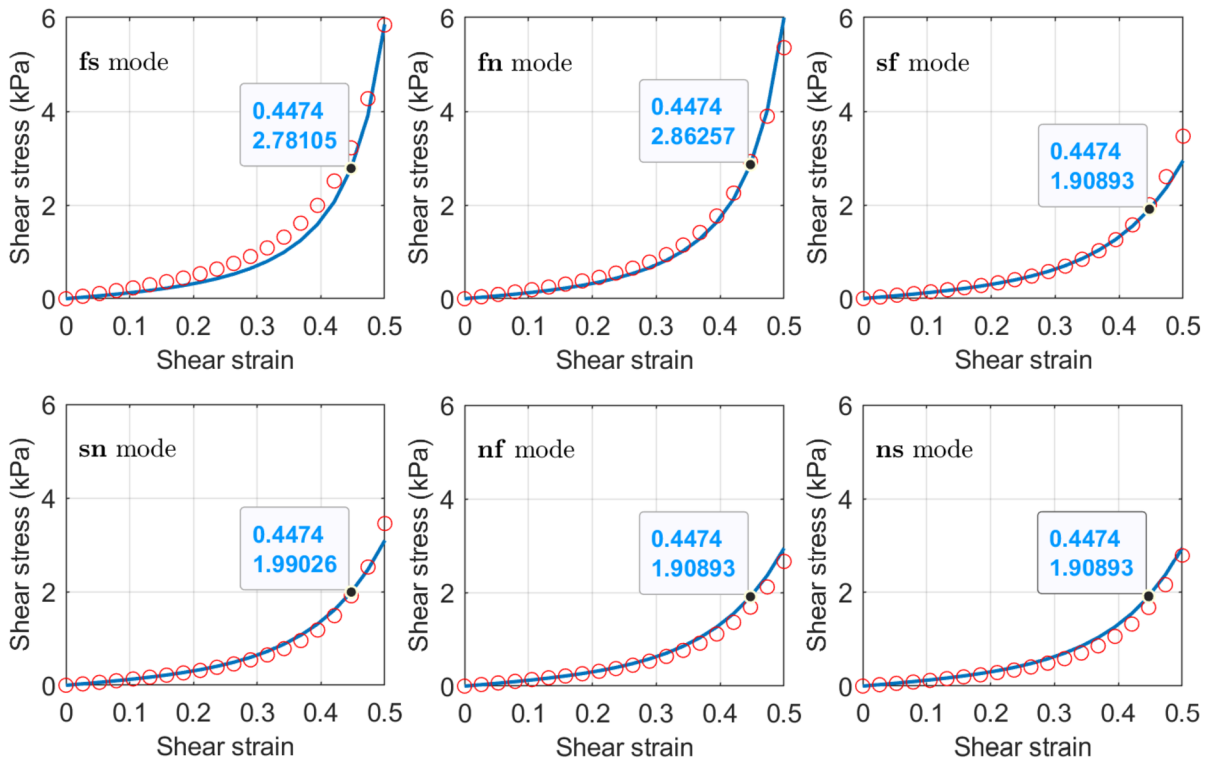
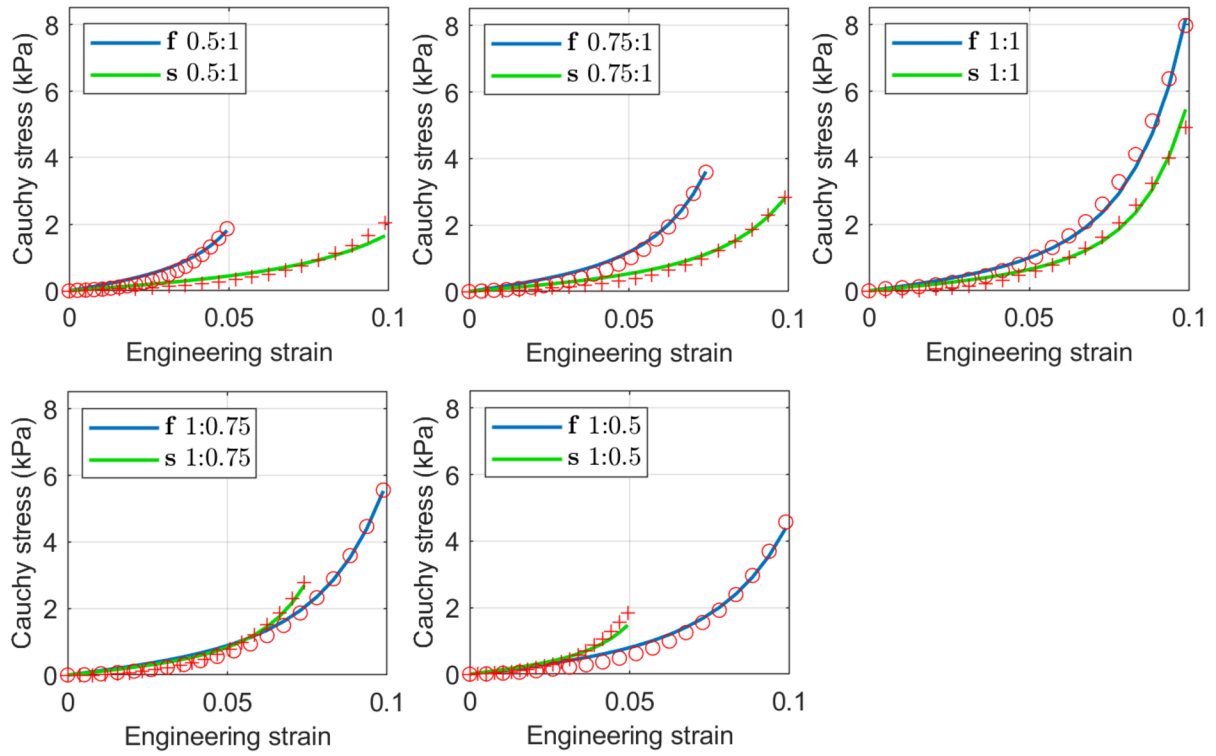


Fig. 7: Fit of the model (4.1) (solid curves) to the experimental data extracted from Sommer et al. [28] (red circles and plus signs). The top 5 graphs show the biaxial responses while the bottom six graphs compare responses to the simple shear tests. The material parameters used are given in Table 4. See Fig. 6 for the explanation of shear modes.

4.2 Inclusion of prestress

The strain-energy function Ψ , defined by (4.1), must be associated with a reference configuration that is stress-free. However, the reference configuration Ω , used in this work, represents LV in its end-diastolic state when the blood pressure of about 2.00 kPa acts on the endocardial surface and, consequently, the ventricular muscle is already stressed. Thus, it is necessary to include prestress into Ω .

An efficient iterative algorithm for inclusion of prestress into FE models was proposed by Maas et al. [33]. The algorithm is based in the more general theory of virtual configurations proposed by Johnson and Hoger [34, 35]. The algorithm replaces the “standard” deformation gradient \mathbf{F} in constitutive equations by the total deformation gradient $\widehat{\mathbf{F}}$ defined by:

$$\widehat{\mathbf{F}} := \mathbf{F}\mathbf{F}_p, \quad (4.6)$$

where \mathbf{F}_p is the *prestrain gradient* which must be iteratively calculated for each integration point of every element in the mesh. In the beginning of solution, \mathbf{F}_p is set equal to the identity tensor \mathbf{I} (i.e. no prestrain is applied). Afterwards, in every iteration, loads (the pressure of 2.00 kPa in the present case) and the current estimate of prestrain gradient field \mathbf{F}_p are applied to the mesh and a standard FE solution is executed. This solution produces new deformation gradients \mathbf{F} (one for each integration point) which are multiplied by \mathbf{F}_p and the resulting tensors $\mathbf{F}_p\mathbf{F}$ are used in the subsequent iteration as new estimates of prestrain gradients. The procedure is terminated when the calculated nodal displacements (upon application of both external loads and the actual prestrain field) are close enough to zero. In this work, the maximum tolerated displacement was chosen to be 0.5 mm.

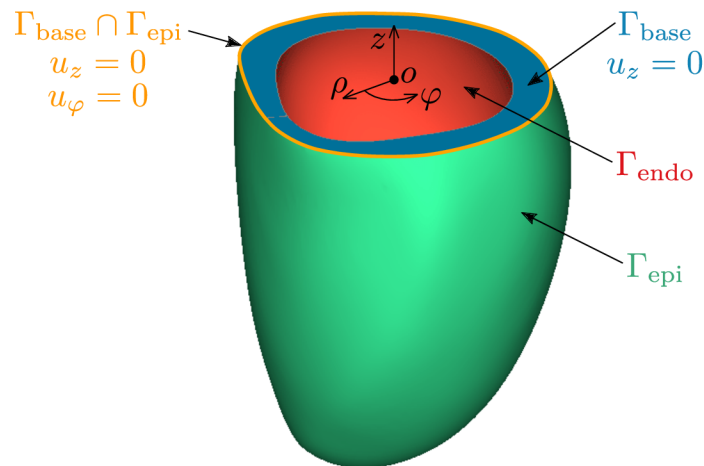


Fig. 8: Displacement boundary conditions on the basal surface Γ_{base} were prescribed in a cylindrical coordinate system (ρ, φ, z) . For all nodes in Γ_{base} , the displacement u_z in z direction was set to zero. Additionally, zero displacement u_φ in the direction tangent to the φ coordinate was prescribed to all *corner* nodes (i.e. not to the nodes in the interior of the edges of elements) situated on the borderline between Γ_{base} and Γ_{epi} (orange contour in the figure).

The algorithm described above had to be slightly modified because of problems with convergency. Also, since the hyperelastic model defined by (4.1) is orthotropic, it was necessary not only to substitute \mathbf{F} by $\widehat{\mathbf{F}}$ in the definition, but also to replace \mathbf{f} and \mathbf{n} in

the definitions of I_4 and K_1 by their counterparts in the virtual stress-free configuration. These issues are discussed in the full version of the thesis.

The final displacements before and after inclusion of prestrain/prestress are shown in Fig. 9. Displacement boundary conditions applied during the solution (and in every other solution presented in this chapter) are shown in Fig. 8. Fig. 10 shows the distribution of the first principal stress in the prestressed configuration.

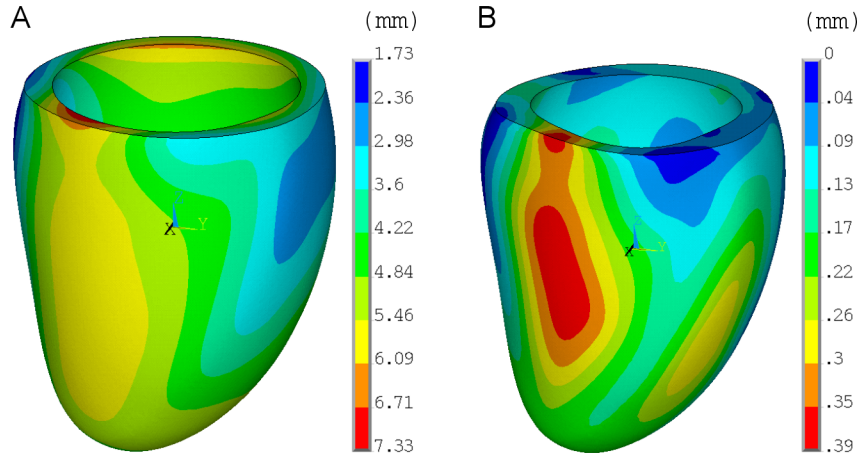


Fig. 9: (A) Total displacements resulting from the application of the end-diastolic pressure of 2 kPa on the endocardial surface of the model with no initial prestress. (B) Total displacements for the same pressure load when iteratively calculated prestrain gradients were applied.

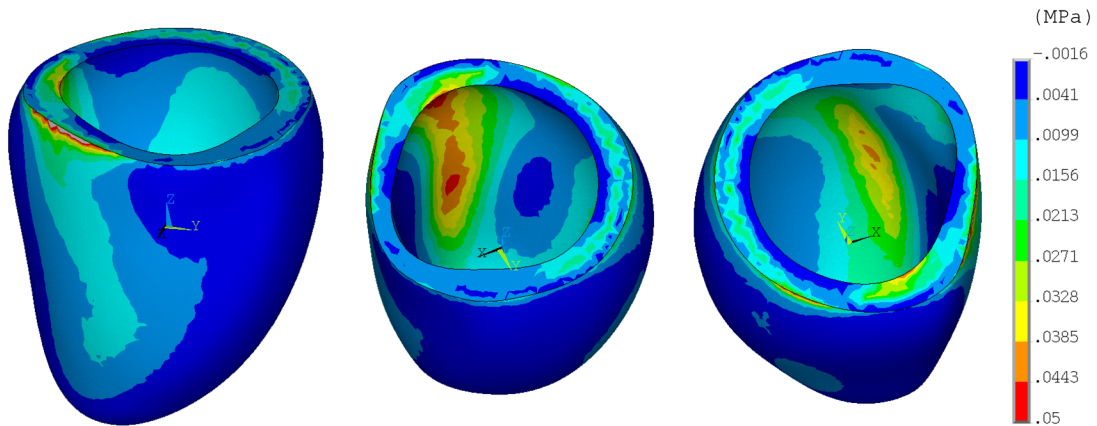


Fig. 10: (A) Calculated distribution of the first principal stress in the prestressed reference configuration (the same one that is shown in Fig. 9B). The upper bound of the contour legend was decreased to 0.050 MPa in order to filter unrealistic stress concentrations near some nodes at the base with imposed displacement boundary conditions and also to obtain a better picture of the stress distribution in other parts of the model (see the full version of the thesis for the original contour plot). Areas with stresses higher than 0.050 MPa are displayed in gray color (this is the case of only one small region in the leftmost figure of panel B).

4.3 Modeling of fibre contraction

The contraction of muscle fibres can be modeled using the *active strain approach* [36, 37] in which the *active strain tensor* \mathbf{F}_a is introduced. It is most often defined in the form [36, 37]:

$$\mathbf{F}_a := \lambda^{-1} \mathbf{f} \otimes \mathbf{f} + \sqrt{\lambda} (\mathbf{s} \otimes \mathbf{s} + \mathbf{n} \otimes \mathbf{n}), \quad (4.7)$$

where λ is the stretch in the fibre direction which must be prescribed. Tensor \mathbf{F}_a , when defined by (4.7), can be seen as a deformation gradient which maps a contracted fibre (which is shortened and widened) back to its resting state (i.e. to its initial length and cross section). The deformation described by (4.7) is transversely isotropic and isochoric ($\det(\mathbf{F}_a) = 1$). In this work, the time-course of λ was defined on the basis of the experimental time-course of unloaded shortening of human myocardial specimen, shown in Fig. 11.

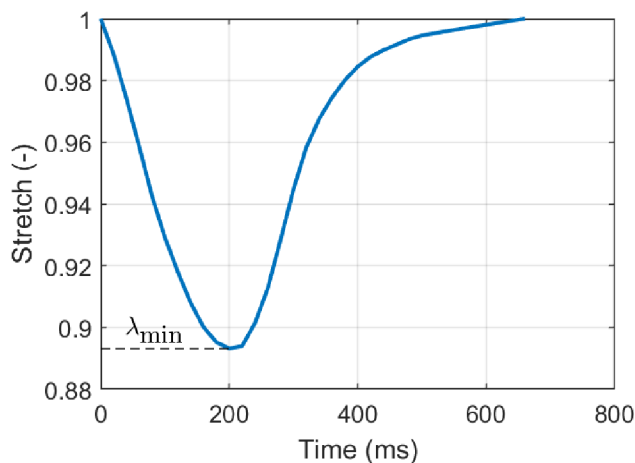


Fig. 11: An evolution of axial stretch λ during an unloaded contraction of a slim myocardial specimen cut from human left ventricle. The graph is based on Fig. 1B of [38]. Since the extent of shortening of the specimen is quite small, the curve had to be scaled in vertical direction before used in the FE model, so as to achieve lower minimum stretch λ_{\min} (i.e. increase the extent of shortening/increase the contractile force). More details are given in the full version of the thesis.

The active strain tensor \mathbf{F}_a can be incorporated into the prestressed constitutive equation, dependent on $\hat{\mathbf{F}}$, by defining another total deformation gradient in the form:

$$\hat{\mathbf{F}}^* := \mathbf{F} \mathbf{F}_a \mathbf{F}_p. \quad (4.8)$$

If \mathbf{F} in the strain-energy function (4.1) is replaced by $\hat{\mathbf{F}}^*$ (and the structural vectors \mathbf{f} and \mathbf{n} are transformed as described in the full version of the thesis), then the resulting constitutive model will include the influence of initial prestrain, and it will also be capable of generating the active tension in the fibre direction (by prescribing \mathbf{F}_a with $\lambda < 1$).

4.4 Specification of simulated conditions

Experiments have shown that there is a delay between the electrical activation of the cardiac muscle cell and its mechanical response (onset of contraction) [39]. Moreover, it was shown that the length of this electromechanical delay changes considerably across the thickness of the wall [39]. Thus, in order to distribute the onset of contraction in the

control and LBBB simulations, it was necessary to calculate the value of the delay for each element in the mesh according to the position of its centroid relative to the endocardial and epicardial surfaces. This calculation was performed in Matlab using the electromechanical delays measured by Cordeiro et al. [39] in cells isolated from subendocardial, middle and subepicardial layers of myocardium. These experimental values were linearly interpolated across the wall of the FE model. The onset of contraction was then calculated for each element in the mesh as the sum of its electrical activation time (taken either from the control or the LBBB simulation) and its electromechanical delay.

Both control and LBBB simulations of LV contraction were governed by the same algorithm, programmed in Ansys APDL, which automatically changed the conditions of simulation according to the phase of the cardiac cycle. In the beginning of solution, the calculated prestrain gradients and the end-diastolic pressure of 2 kPa were applied on the model. When the elements started to contract, the isovolumic contraction phase began. During this phase the volume of the ventricle had to be kept approximately constant; thus in each time step it was necessary to iteratively calculate the value of the endocardial pressure for which this condition was satisfied. When the rising LV pressure exceeded 10.6 kPa (the diastolic pressure), the ejection phase started during which the endocardial pressure was controlled by the two-element Windkessel model [40]. Parameters of the model (the arterial compliance C_w and the total peripheral resistance R_w) were tuned to give a realistic pressure and volume waveforms. During the ejection phase the volume of the ventricle gradually decreased. When it started increasing (reversed blood flow), the ejection phase was immediately terminated and the solution continued with the isovolumic relaxation phase which was modeled in the same way as the isovolumic contraction phase. Isovolumic relaxation was terminated when the pressure decreased below 1.8 kPa (left atrial pressure at the end of isovolumic relaxation [41]). The subsequent phase of ventricular filling was modeled in a very simple manner by prescribing a linear increase of pressure back to its end-diastolic value of 2 kPa.

The control and the LBBB simulation differed only in the prescribed electrical (and thus also mechanical) activation times; all other parameters controlling the evolution of pressure and volume were identical in both simulations.

4.5 Results

Calculated pressure and volume waveforms for the control and the LBBB conditions are compared in Fig. 12. It can be seen that after the prescription of the activation pattern representing the LBBB, the systolic pressure (peak pressure on the pressure curves) decreased by 4.4 % and the ejection fraction decreased by 2.3 % (from 63.2 % to 60.9 %). This decrease in ejection fraction is similar to that reported by Özdemir et al. [5] and Aalen et al. [8] who observed 4% decrease in patients with LBBB. The curves from Fig. 12 were used to construct the pressure-volume diagrams shown in Fig. 13.

Changes in LV motions, caused by the LBBB, are manifested by enlarged displacements of the ventricular apex in directions perpendicular to the long axis of the ventricle [9, 10]. Fig. 14 shows that these changes are captured also by the FE model. Moreover, the calculated strain waveforms displayed in Fig. 15 demonstrate that contraction of the lateral wall of the ventricle is markedly delayed compared to the septal contraction, which is in agreement with magnetic resonance-based strain measurements in dogs with induced LBBB [42].

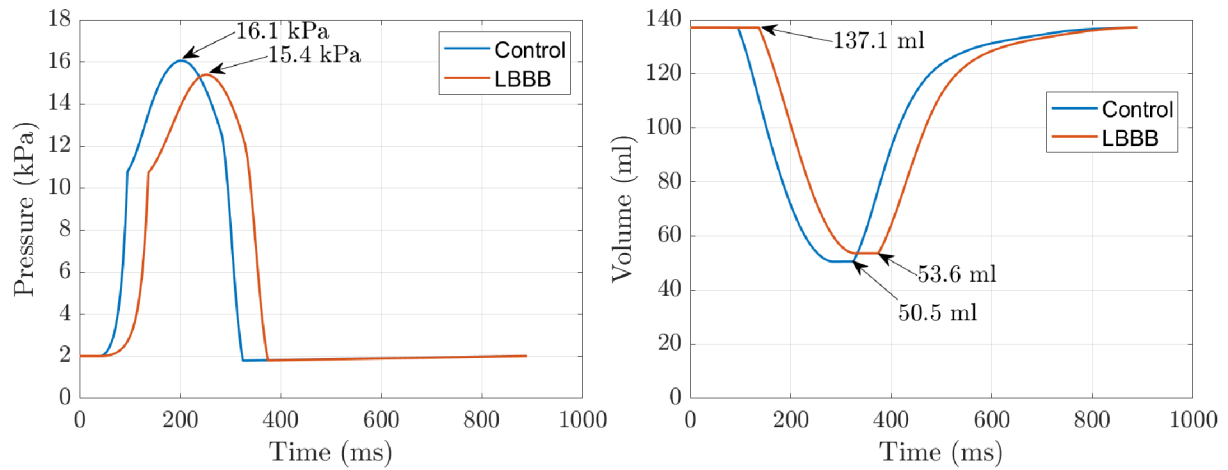


Fig. 12: Calculated pressures and volumes representing a healthy ventricle (Control) and a ventricle with the left bundle branch block (LBBB).

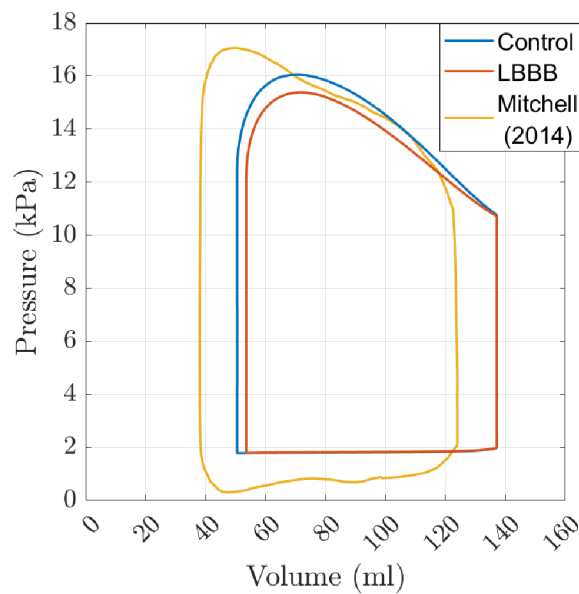


Fig. 13: Calculated pressure-volume diagrams representing a healthy ventricle (Control) and a ventricle with the left bundle branch block (LBBB). The diagrams are compared with a real one constructed from the pressure and volume waveforms taken from the paper by Mitchell and Wang (2014) [41].

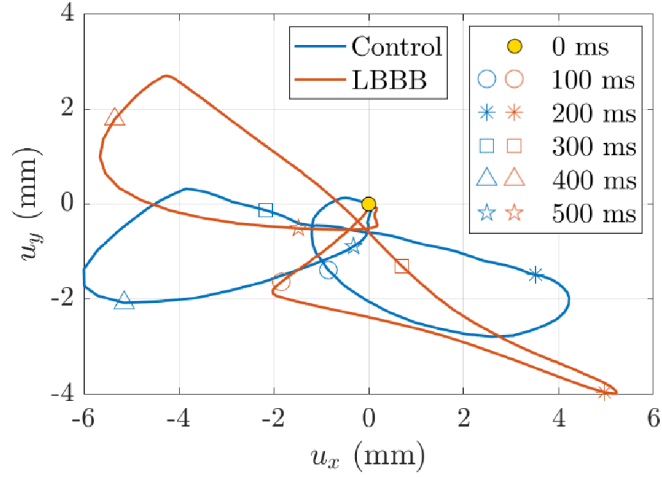


Fig. 14: Displacements u_x and u_y (corresponding to the global x and y directions, see Figs. 4 and 5) of the lowest apical node in the FE model during the whole cardiac cycle. Results are shown for a healthy ventricle (Control) and for a ventricle with the left bundle branch block (LBBB). Markers denote selected times within the cardiac cycle (values correspond to the timeline in Fig. 12).

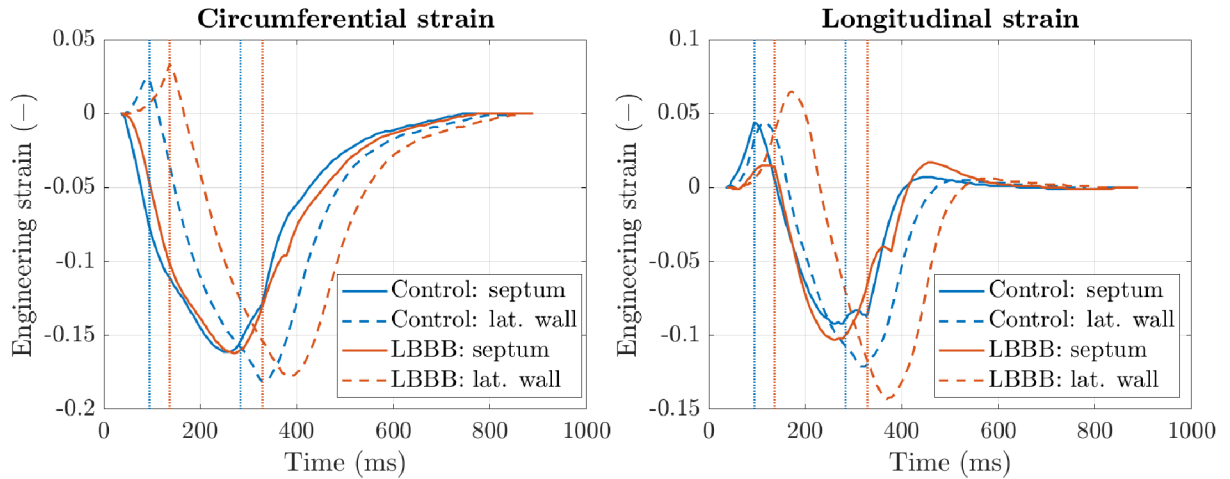


Fig. 15: Temporal evolution of circumferential and longitudinal strains in the central part of the right septal surface and in the site across the diameter of the ventricle on the epicardial surface of the lateral wall. Results are shown for a healthy ventricle (Control) and for a ventricle with the left bundle branch block (LBBB). Vertical lines mark the beginning and the end of ejection phase for each simulation. Timeline is the same as in Fig. 12.

The last quantity that should be analyzed in this work, according to the goals specified in Chapter 2, is wall stress. Stresses at the end of diastole were already discussed in Sec. 4.2. Figs. 16, 17 and 18 below show the distribution of the first principal stress at another three characteristic stages of the cardiac cycle, namely: the beginning of ejection, the moment when the LV pressure reaches its peak, and the end of ejection. Just like in Fig. 10 of Sec. 4.2, unrealistic stress concentrations near the base were excluded from the plots by restricting the intervals of the contour legends.

At the beginning of ejection (Fig. 16), the stress distribution is almost uniform in the anterior, lateral and posterior regions of the ventricle, especially on the epicardial surface. But this uniformity is totally disrupted in the septum where much higher stresses are concentrated in a narrow band running obliquely across the right septal surface from the base toward the apex. These concentrations are more pronounced in the LBBB simulation which is probably because ejection is delayed in this case which means that the early-activated septum have more time to increase the active stresses. However, it must be admitted that the accuracy of stresses calculated in the septum and adjacent regions is somewhat questionable because this study neglected the forces exerted on the septum by the contracting right ventricle (e.g. the right ventricular pressure acting on the right septal surface was not taken into consideration).

The moment of peak LV pressure (Fig. 17) is characterized by “banded” stress distribution which is obviously largely dependent on the prescribed fibre directions. Stress values in the anterior, lateral and posterior regions of the ventricle are less uniform than in the previous case. On the right septal surface there is again the band with concentrated high stresses, but this time the stress values are comparable for both simulations.

The dependence on the fibre directions can be recognized also in the stress field at the end of ejection (Fig. 18). Substantially increased septal stresses at this moment can be seen only in the control simulation; in the model with the LBBB, the septum is already relaxing and so the stresses are reduced.

It should be noted that the calculated stresses shown in the figures are generally far higher than those for which the hyperelastic model was calibrated. Therefore, it is doubtful whether the predicted responses, calculated for strains that are very far from available experimental data, are reliable. Unfortunately, this is an inherent disadvantage of the active strain approach in which a single (total) stress tensor is derived from a particular strain-energy function which, however, is never designed to reproduce the active stresses. This disadvantage can be eliminated by using an alternative *active stress approach* [36, 37] for modeling of contractile tissues. This approach was, in fact, the first choice for this thesis, but the implemented algorithm suffered from severe convergence difficulties during the ejection phase that could not be overcome. For this reason, the active strain formulation was eventually used which turned out to be numerically more stable.

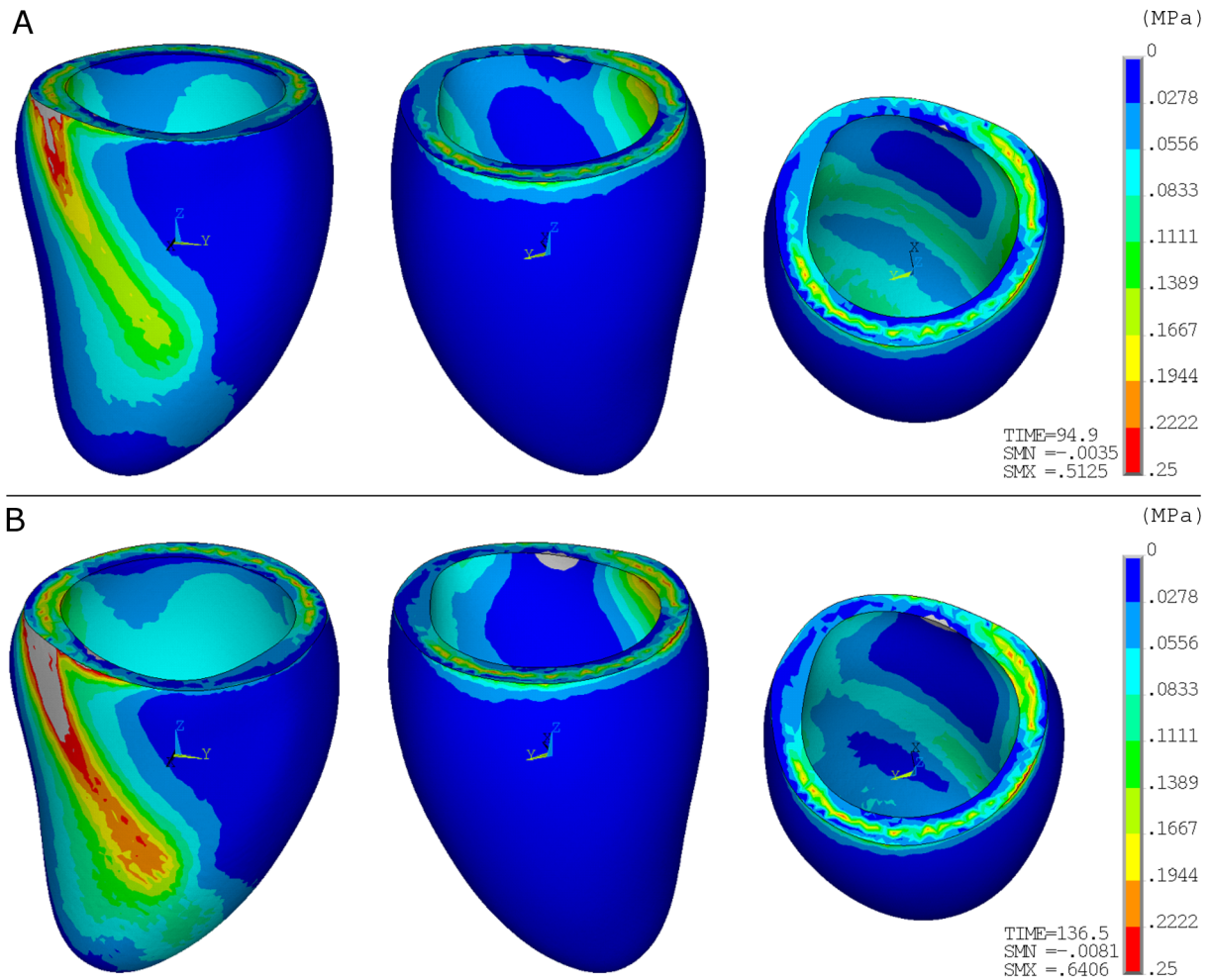


Fig. 16: Calculated distribution of the first principal stress at the beginning of ejection (A: control simulation, B: LBBB simulation). Upper bound of the contour legend was decreased to 0.25 MPa in order to remove unrealistic stress concentrations near the basal nodes with prescribed displacement boundary conditions. Lower bound of the legend was increased to 0 MPa so that both panels, A and B, use the same contour lines (for better comparison). Stresses outside the specified interval are shown in gray color. The actual calculated maximum and minimum stress values are written at the bottom of the legend along with the precise time of the beginning of ejection.

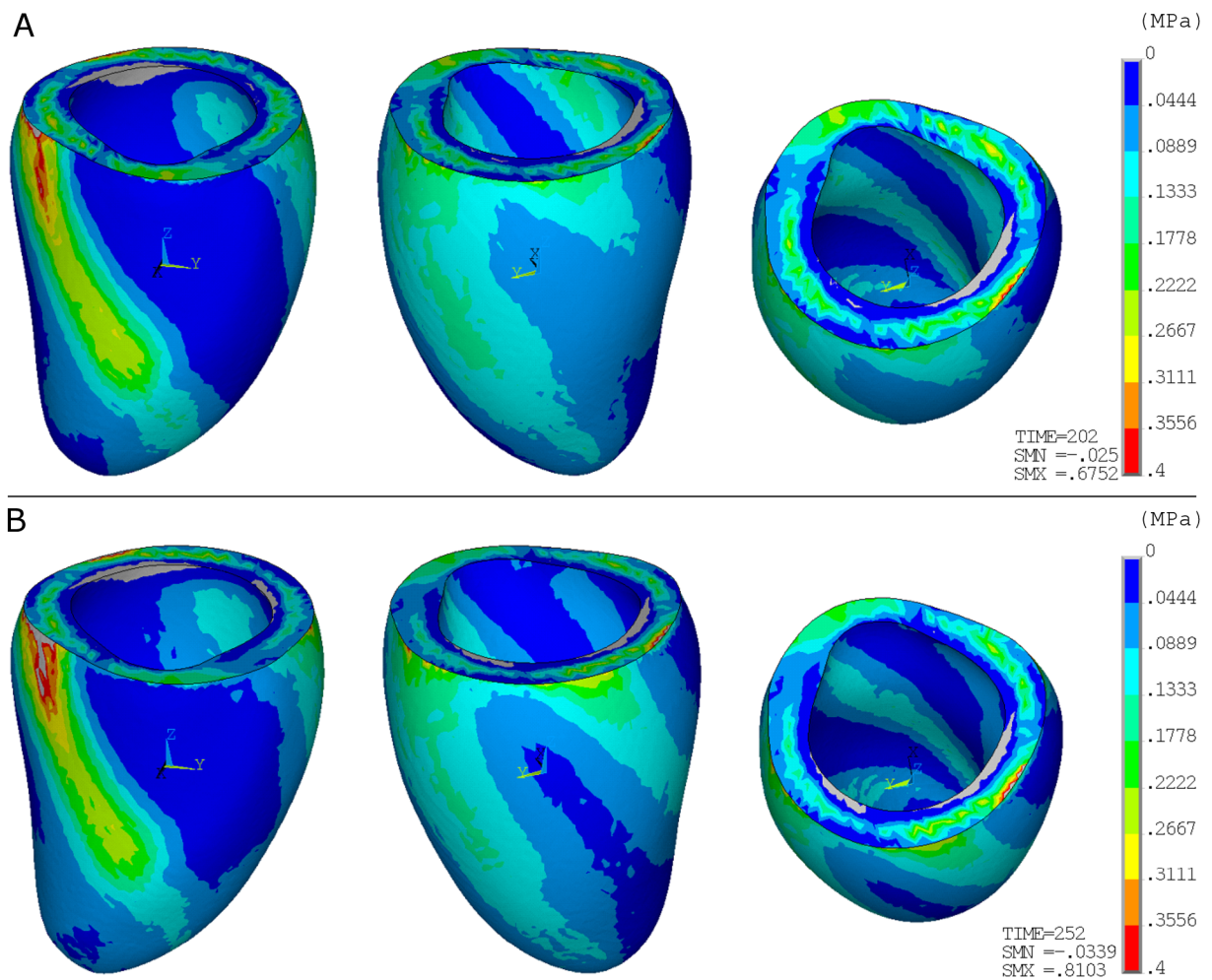


Fig. 17: Calculated distribution of the first principal stress at the moment when the LV pressure reaches its peak (A: control simulation, B: LBBB simulation). Upper bound of the contour legend was decreased to 0.4 MPa in order to remove unrealistic stress concentrations near the basal nodes with prescribed displacement boundary conditions. Lower bound of the legend was increased to 0 MPa so that both panels, A and B, use the same contour lines (for better comparison). Stresses outside the specified interval are shown in gray color. The actual calculated maximum and minimum stress values are written at the bottom of the legend along with the precise time when the peak pressure was reached.

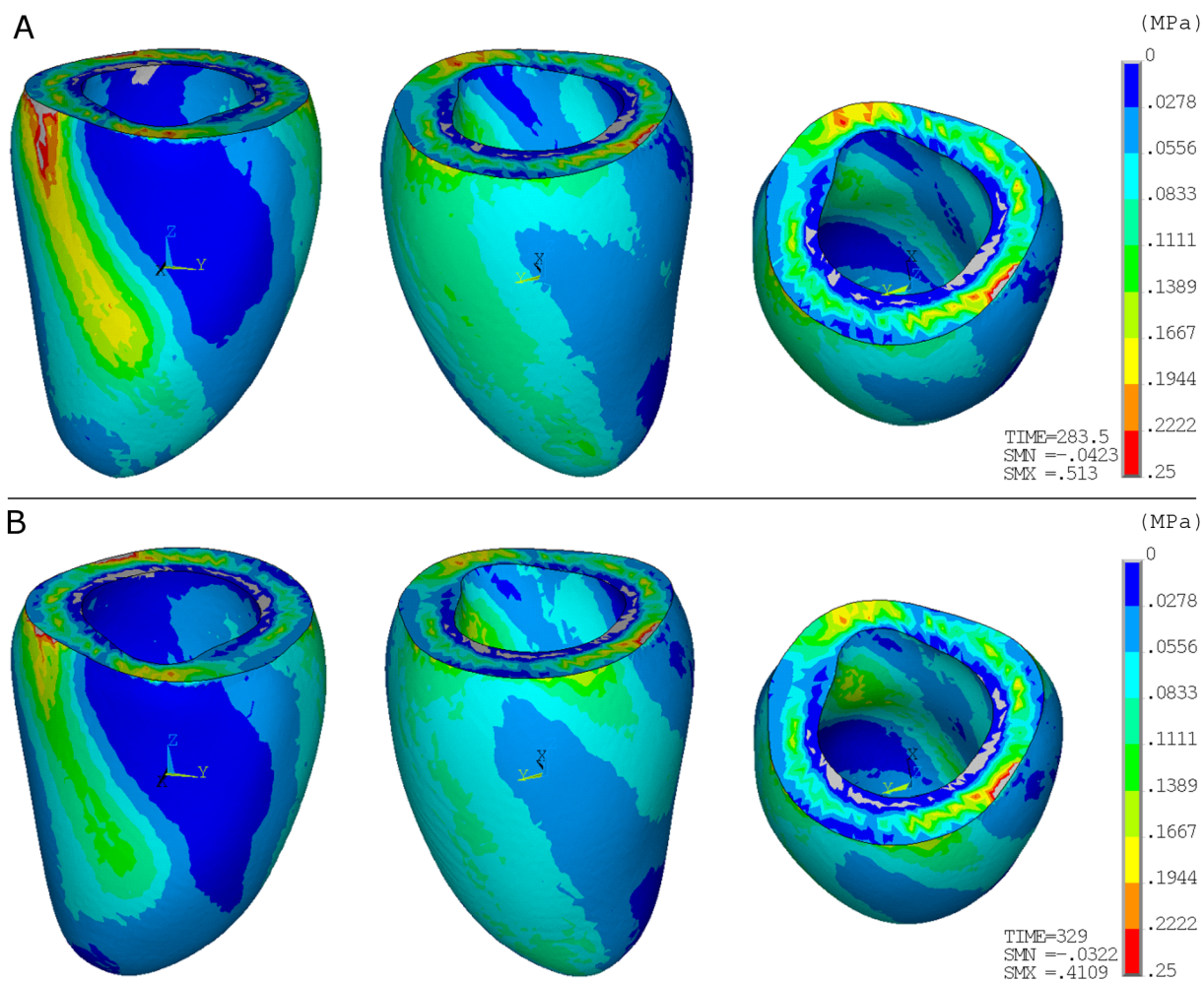


Fig. 18: Calculated distribution of the first principal stress at the end of ejection (A: control simulation, B: LBBB simulation). Upper bound of the contour legend was decreased to 0.25 MPa in order to remove unrealistic stress concentrations near the basal nodes with prescribed displacement boundary conditions. Lower bound of the legend was increased to 0 MPa so that both panels, A and B, use the same contour lines (for better comparison). Stresses outside the specified interval are shown in gray color. The actual calculated maximum and minimum stress values are written at the bottom of the legend along with the precise time of the end of ejection.

5 Conclusion

Simulations of the left ventricular contraction presented in this thesis indicate that the LBBB alone does not substantially reduce the pumping efficiency of the ventricle. When a normal electrical activation sequence was replaced by that representing the LBBB, the ejection fraction decreased by only 2.3 %, despite the fact that the total electrical activation time was prolonged by 50 %.

Mechanical consequences of the block were assessed by analyzing displacements of ventricular apex along with wall strains in the septum and in the lateral wall of the ventricle. These analyses confirmed that the model captures some basic characteristics of the LBBB-induced mechanical dyssynchrony, reported in literature. Specifically, apical displacements were increased in the presence of the block and strain analysis demonstrated delayed contraction of the lateral wall relative to the septum.

Stresses were analyzed at four characteristic instants within the cardiac cycle: the end of diastole, the beginning of ejection, the moment when the blood pressure reaches its peak (i.e. the systolic pressure), and the end of ejection. At all these stages, significantly higher stresses were observed in or around the septum than in the rest of the model. It is, however, questionable whether such high stresses truly exist in a beating heart in which the stress distribution is surely influenced by forces arising from the right ventricular contraction, which were neglected in the present study (as they were in many other studies that modeled only the left ventricle, isolated from its surroundings [20, 18, 43, 44]). However, the results presented in this work suggest that it could be beneficial to take these interactions between the left and the right ventricle into consideration in the future; at least the right ventricular blood pressure should be applied on the right septal surface and the results compared with those presented here.

In regions outside the septum, the stress pattern was markedly influenced by the prescribed fibre directions which emphasizes how important it is to describe the mechanical behavior of myocardium by anisotropic constitutive equations, and to respect the arrangement of fibres in ventricular walls. Interestingly, stress magnitudes were not considerably different in control and LBBB simulations, except for the septum.

Besides the ignored influence of the right ventricle, several other shortcomings of the model are discussed in the full version of the thesis. The strain-energy function proposed in Sec. 4.1, although seemingly suitable for modeling biaxial and simple shear responses, does not correctly order the simple shear modes according to their stiffness. This inconsistency of the constitutive model is barely perceptible in the present case, but the suitability of the model for the description of myocardial behavior is challenged by this fact. Inaccuracies were also recognized on the simulated LV pressure curves. The calculated pressure rise during isovolumic contraction is not entirely realistic, even though the total duration of the isovolumic contraction phase corresponds well with clinical measurements for both control and LBBB conditions. Also, the ejection phase is too short in both simulations which is most likely an inherent drawback of the two-element Windkessel model which was used to calculate the pressure boundary condition during the ejection phase.

These shortcomings identify some potential directions for future improvement.

References

- [1] Macfarlane PW, van Oosterom A, Pahlm O, Kligfield P, Janse M, Camm J. Comprehensive Electrocardiology. 6th ed. Springer London; 2010.
- [2] Smiseth OA, Aalen JM. Mechanism of harm from left bundle branch block. Trends in Cardiovascular Medicine. 2019;29(6):335-42.
- [3] Cikes M, Solomon SD. Beyond ejection fraction: an integrative approach for assessment of cardiac structure and function in heart failure. European Heart Journal. 2015 09;37(21):1642-50.
- [4] Grines CL, Bashore TM, Boudoulas H, Olson S, Shafer P, Wooley CF. Functional abnormalities in isolated left bundle branch block. The effect of interventricular asynchrony. Circulation. 1989;79(4):845-53.
- [5] Özdemir K, Altunkeser BB, Daniş G, Özdemir A, Uluca Y, Tokaç M, et al. Effect of the isolated left bundle branch block on systolic and diastolic functions of left ventricle. Journal of the American Society of Echocardiography. 2001;14(11):1075-9.
- [6] Valenti V, Zia MI, Shubayev L, Edelstein S, Supariwala A, Uretsky S, et al. Cardiac Magnetic Resonance Evaluation of the Impact of Interventricular and Intraventricular Dyssynchrony on Cardiac Ventricular Systolic and Diastolic Function in Patients With Isolated Left Bundle Branch Block. The American Journal of Cardiology. 2012;110(11):1651-6.
- [7] Akhtari S, Chuang M, Salton C, Berg S, Kissinger K, Goddu B, et al. Effect of isolated left bundle-branch block on biventricular volumes and ejection fraction: a cardiovascular magnetic resonance assessment. J Cardiovasc Magn Reson. 2018;20(66).
- [8] Aalen J, Storsten P, Remme EW, Sirnes PA, Gjesdal O, Larsen CK, et al. Afterload Hypersensitivity in Patients With Left Bundle Branch Block. JACC: Cardiovascular Imaging. 2019;12(6):967-77.
- [9] Voigt JU, Schneider TM, Korder S, Szulik M, Gürel E, Daniel WG, et al. Apical transverse motion as surrogate parameter to determine regional left ventricular function inhomogeneities: a new, integrative approach to left ventricular asynchrony assessment. European Heart Journal. 2009 03;30(8):959-68.
- [10] Stankovic I, Prinz C, Ciarka A, Daraban AM, Kotrc M, Aaronson M, et al. Relationship of visually assessed apical rocking and septal flash to response and long-term survival following cardiac resynchronization therapy (PREDICT-CRT). European Heart Journal - Cardiovascular Imaging. 2015 11;17(3):262-9.
- [11] Vaverka J, Burša J, Šumbera J, Pásek M. Effect of Transmural Differences in Excitation-Contraction Delay and Contraction Velocity on Left Ventricle Isovolumic Contraction: A Simulation Study. BioMed Research International. 2018;2018.
- [12] Vaverka J, Moudr J, Lokaj P, Burša J, Pásek M. Impact of Decreased Transmural Conduction Velocity on the Function of the Human Left Ventricle: A Simulation Study. BioMed Research International. 2020;2020.

- [13] Bai W, Shi W, de Marvao A, Dawes TJW, O'Regan DP, Cook SA, et al. A bi-ventricular cardiac atlas built from 1000+ high resolution MR images of healthy subjects and an analysis of shape and motion. *Medical Image Analysis*. 2015;26(1):133-45.
- [14] Fenton F, Karma A. Vortex dynamics in three-dimensional continuous myocardium with fiber rotation: Filament instability and fibrillation. *Chaos: An Interdisciplinary Journal of Nonlinear Science*. 1998;8(1):20-47.
- [15] Caldwell BJ, Trew ML, Sands GB, Hooks DA, LeGrice IJ, Smaill BH. Three Distinct Directions of Intramural Activation Reveal Nonuniform Side-to-Side Electrical Coupling of Ventricular Myocytes. *Circulation: Arrhythmia and Electrophysiology*. 2009;2(4):433-40.
- [16] Clayton RH, Bernus O, Cherry EM, Dierckx H, Fenton FH, Mirabella L, et al. Models of cardiac tissue electrophysiology: Progress, challenges and open questions. *Progress in Biophysics and Molecular Biology*. 2011;104(1):22-48.
- [17] Holzapfel GA, Ogden RW. Constitutive modelling of passive myocardium: a structurally based framework for material characterization. *Philosophical Transactions of the Royal Society A: Mathematical, Physical and Engineering Sciences*. 2009;367(1902):3445-75.
- [18] Gerbi A, Dedè L, Quarteroni A. A monolithic algorithm for the simulation of cardiac electromechanics in the human left ventricle. *Mathematics in Engineering*. 2019;1(1):1-37.
- [19] Quarteroni A, Valli A. *Numerical Approximation of Partial Differential Equations*. Springer-Verlag; 1994.
- [20] Quarteroni A, Lassila T, Rossi S, Ruiz-Baier R. Integrated Heart—Coupling multi-scale and multiphysics models for the simulation of the cardiac function. *Computer Methods in Applied Mechanics and Engineering*. 2017;314:345-407.
- [21] Ciarlet PG. *The Finite Element Method for Elliptic Problems*. Classics in Applied Mathematics. Society for Industrial and Applied Mathematics; 2002.
- [22] Agger P, Ilkjær C, Laustsen C, Smerup M, Frandsen J, Ringgaard S, et al. Changes in overall ventricular myocardial architecture in the setting of a porcine animal model of right ventricular dilation. *Journal of Cardiovascular Magnetic Resonance*. 2017 12;19.
- [23] Stephenson R, Atkinson A, Kottas P, Filip P, Jafarzadeh F, Bateman M, et al. High resolution 3-Dimensional imaging of the human cardiac conduction system from microanatomy to mathematical modeling. *Scientific Reports*. 2017 12;7.
- [24] Durrer D, van Dam RT, Freud GE, Janse MJ, Meijler FL, Arzbaecher RC. Total Excitation of the Isolated Human Heart. *Circulation*. 1970;41(6):899-912.
- [25] Kléber AG, Janse MJ, Fast VG. In: *Normal and Abnormal Conduction in the Heart*. John Wiley & Sons, Ltd; 2011. p. 455-530.

- [26] Grant RP, Dodge HT. Mechanisms of QRS complex prolongation in man: Left ventricular conduction disturbances. *The American Journal of Medicine*. 1956;20(6):834-52.
- [27] Yin FCP, Strumpf RK, Chew PH, Zeger SL. Quantification of the mechanical properties of noncontracting canine myocardium under simultaneous biaxial loading. *Journal of Biomechanics*. 1987;20(6):577-89.
- [28] Sommer G, Schriebl AJ, Andrä M, Sacherer M, Viertler C, Wolinski H, et al. Biomechanical properties and microstructure of human ventricular myocardium. *Acta Biomaterialia*. 2015;24:172-92.
- [29] Dokos S, Smaill B, Young A, Legrice I. Shear properties of passive ventricular myocardium. *American journal of physiology Heart and circulatory physiology*. 2003 01;283:H2650-9.
- [30] Balzani D, Neff P, Schröder J, Holzapfel GA. A polyconvex framework for soft biological tissues. Adjustment to experimental data. *International Journal of Solids and Structures*. 2006;43(20):6052-70.
- [31] Steigmann D. Frame-invariant polyconvex strain-energy functions for some anisotropic solids. *Mathematics and Mechanics of Solids*. 2003 10;8:497-506.
- [32] Ansys 2021 R1: Programmer's Reference. ANSYS Inc., Canonsburg, Pennsylvania;. <http://www.ansys.com>.
- [33] Maas S, Erdemir A, Halloran J, Weiss J. A General Framework for Application of Prestrain to Computational Models of Biological Materials. *Journal of the Mechanical Behavior of Biomedical Materials*. 2016 04;61.
- [34] Johnson BE, Hoger A. The use of a virtual configuration in formulating constitutive equations for residually stressed elastic materials. *Journal of Elasticity*. 1995;41:177-215.
- [35] Hoger A. Virtual Configurations and Constitutive Equations for Residually Stressed Bodies with Material Symmetry. *Journal of Elasticity*. 1997;48:125-44.
- [36] Giansesio G, Musesti A, Riccobelli D. A Comparison Between Active Strain and Active Stress in Transversely Isotropic Hyperelastic Materials. *Journal of Elasticity*. 2019 10.
- [37] Pezzuto S, Ambrosi D, Quarteroni A. An orthotropic active-strain model for the myocardium mechanics and its numerical approximation. *European Journal of Mechanics - A/Solids*. 2014 11;48.
- [38] Holubarsch C, Lüdemann J, Wiessner S, Ruf T, Schulte-Baukloh H, Schmidt-Schweda S, et al. Shortening versus isometric contractions in isolated human failing and non-failing left ventricular myocardium: dependency of external work and force on muscle length, heart rate and inotropic stimulation. *Cardiovascular Research*. 1998 01;37(1):46-57.

- [39] Cordeiro JM, Greene L, Heilmann C, Antzelevitch D, Antzelevitch C. Transmural heterogeneity of calcium activity and mechanical function in the canine left ventricle. *American Journal of Physiology-Heart and Circulatory Physiology*. 2004;286(4):H1471-9.
- [40] Stergiopoulos N, Meister JJ, Westerhof N. Evaluation of methods for estimation of total arterial compliance. *The American journal of physiology*. 1995;268 4 Pt 2:H1540-8.
- [41] Mitchell J, Wang JJ. Expanding application of the Wiggers diagram to teach cardiovascular physiology. *Advances in physiology education*. 2014 06;38:170-5.
- [42] Byrne MJ, Helm RH, Daya S, Osman NF, Halperin HR, Berger RD, et al. Diminished Left Ventricular Dyssynchrony and Impact of Resynchronization in Failing Hearts With Right Versus Left Bundle Branch Block. *Journal of the American College of Cardiology*. 2007;50(15):1484-90.
- [43] Eriksson T, Prassl A, Plank G, Holzapfel G. Influence of myocardial fiber/sheet orientations on left ventricular mechanical contraction. *Mathematics and Mechanics of Solids*. 2013;18(6):592-606.
- [44] Eriksson T, Prassl A, Plank G, Holzapfel G. Modeling the dispersion in electromechanically coupled myocardium. *International journal for numerical methods in biomedical engineering*. 2013 01;29:1267-84.

Curriculum vitae

Personal details

Name Jiří Vaverka
Date of birth 4. 6. 1992
Address Sobůlky 123, 697 01 Kyjov
E-mail jiri.vaverka15@gmail.com

Education

2016 – present Applied Mechanics (doctoral study)
Brno University of Technology
Faculty of Mechanical Engineering

2014 – 2016 Engineering Mechanics and Biomechanics (Master’s degree)
Brno University of Technology
Faculty of Mechanical Engineering

2011 – 2014 Mechanical Engineering (Bachelor’s degree)
Brno University of Technology
Faculty of Mechanical Engineering

Career overview

10/2020 – present Assistant professor
Institute of Solid Mechanics, Mechatronics and Biomechanics
Faculty of Mechanical Engineering
Brno University of Technology

Languages

English (level B2)

Computer skills

Ansys APDL, Matlab, Fortran, Autodesk AutoCAD and Inventor, \LaTeX

Abstract

This doctoral thesis deals with computational modeling of contraction of human left ventricle using finite element method. The primary goal is to determine the impact of the left bundle branch block on ventricular ejection fraction. Additionally, changes in ventricular motions, strains and stress distribution, resulting from the block, are also investigated. Electrical activation of left ventricle under healthy conditions and during the branch block is modeled by the monodomain equation coupled with an artificial ionic model designed to reduce computational demands of the monodomain equation. Conduction velocity in myocardium is considered orthotropic. Calculated activation maps show that the left bundle branch block prolongs electrical activation by 50 % which agrees with clinically observed prolongation of the QRS complex on ECG. The activation maps are subsequently used in the simulations of ventricular mechanics to distribute the beginning of contraction throughout the finite-element mesh. Passive mechanical behavior of myocardium is described by an orthotropic hyperelastic model. Active stresses, induced by muscle contraction, are incorporated by means of the time-dependent active strain tensor. Contraction starts from a prestressed reference configuration representing the end-diastolic state of the ventricle. Pressure development during ejection phase is controlled by two-parametric Windkessel model. Results indicate that the left bundle branch block does not substantially reduce the pumping efficiency of the ventricle; ejection fraction in the diseased state decreased by only 2.3 % relative to the healthy conditions which agrees with some of the previously published clinical studies. Changes in displacements and strains, predicted by the model, correspond with clinical and experimental observations. Stress analyses revealed unexpectedly high stresses in the interventricular septum; further analyses with modified boundary conditions have been suggested in order to better assess these result.

Abstrakt

Tato disertační práce se zabývá výpočtovým modelováním kontrakce levé srdeční komory pomocí metody konečných prvků. Primárním cílem práce je vyhodnotit vliv blokády levého Tawarova raménka na ejekční frakci komory. Dále je vyšetřován dopad blokády na pohyby komory během srdečního cyklu, na lokální hodnoty přetvoření a na rozložení napětí ve stěně. Průběh elektrické aktivace jak zdravé komory, tak i komory s blokádou je modelován pomocí monodoménové rovnice svázané s pseudo-modelem buněčné membrány, který byl navržen za účelem snížení výpočetní náročnosti monodoménové rovnice. Rychlost šíření vzruchu v myokardu je uvažována ortotropní. Vypočítané časové průběhy elektrické aktivace ukazují, že blokáda levého Tawarova raménka prodlužuje dobu depolarizace komory o 50 %, což je v souladu s udávanými délkami trvání QRS komplexu na EKG u zdravých jedinců a u pacientů s blokádou. Průběhy elektrické aktivace jsou následně využity v simulacích kontrakce komory pro předepsání počátku kontrakce jednotlivých prvků sítě. Pasivní mechanická odezva myokardu je v těchto simulacích popsána pomocí ortotropního hyperelastického modelu. Aktivní napětí vyvolané svalovou kontrakcí je do modelu zahrnuto prostřednictvím časově závislého tenzoru aktivního přetvoření. Do počáteční konfigurace modelu, reprezentující stav komory na konci diastoly, je před zahájením kontrakce zahrnuto předpětí odpovídající end-diastolickému tlaku v komoře. Časový průběh komorového tlaku během ejekční fáze je modelován pomocí dvouparametrického modelu Windkessel. Výsledky simulací ukazují, že blokáda levého

Tawarova raménka nesnižuje významně čerpací schopnost komory. Predikovaný pokles ejekční frakce v důsledku blokády činí pouze 2.3 %, což je v souladu s některými publikovanými klinickými výsledky. Vypočítané časové průběhy posuvů a přetvoření ve vybraných místech modelu taktéž vykazují některé charakteristiky popisované klinickými nebo experimentálními studii. V oblasti mezikomorového septa byly pozorovány výrazně vyšší hodnoty napětí než v ostatních částech komory; tyto výsledky však bude nutné ověřit dalšími výpočty, neboť v současném modelu není septum zatíženo silovými účinky vyvolanými kontrakcí pravé komory.